A FLUX COMPARISON OF NORTHERN AND SOUTHERN SATURN KILOMETRIC RADIO BURSTS DURING SOUTHERN SUMMER

Y. Kasaba*, T. Kimura†, D. Maruno*, A. Morioka*,
B. Cecconi‡, L. Lamy‡, C.M. Jackman§, C. Tao¶,
H. Kita*, H. Misawa*, T. Tsuchiya*, and A. Kumamoto*

Abstract

The energy flux of the northern (N–) and southern (S–) Saturn kilometric radiation (SKR) bursts are statistically compared. We investigated the N– and S–SKR bursts from 2005 DOY 250 to 2006 DOY 200, when Cassini was close to the equatorial plane and RPWS could simultaneously observe both N– and S–SKR. We identified 38 burst events, and compared their flux from southern (summer–side) and northern (winter–side) hemispheres. In the main band (100–400 kHz), S–SKR bursts from the summer–side hemisphere were 5–6 times stronger than the N–SKR bursts from the winter–side. This is not far from the flux ratio in the non-burst status. In the low-frequency extension (10–50 kHz) of SKR bursts, this ratio is smaller, about 2–3 times.

1 Introduction

Saturn kilometric radiation (SKR) is observed at 10–1200 kHz in the extraordinary mode, right-hand circularly polarized with respect to the local magnetic field. As a result, SKR from the northern (N–) and southern (S–) polar regions is right-hand (RH) and left-hand (LH) polarized, respectively [Lamy et al., 2008; and references therein], allowing distinguishing N– and S–SKR emissions by the sense of circular polarization.

The Cassini observations before the equinox (11 August 2009) revealed that the N– and S–SKR had different rotational periods of approximately 10.6 and 10.8 h, respectively, which became closer with the approach of the equinox [Kurth et al., 2008; Gurnett et al.,

* *Tohoku University, Sendai, Miyagi, Japan*
† *RIKEN, Wako, Saitama, Japan*
‡ *LESIA, Observatoire de Paris, Meudon, France*
§ *University of Southampton, Southampton, UK*
¶ *National Institute of Information and Communications Technology, Koganei, Tokyo, Japan*

2009]. Based on this asymmetry in the periodic modulations, two SKR phase systems, N– and S–SKR phases, were introduced [Gurnett et al., 2011]. A north–south asymmetry was also found in the SKR energy flux. Lamy et al. [2008] showed that the S–SKR power was larger than N-SKR in 2005 DOY 254 – 2006 DOY 199. Kimura et al. [2013] then showed that the flux ratio of S–SKR to N–SKR was as high as 100 during the end of 2004 and then gradually decreased to 2 around the equinox. Those authors suggest that the variation of the solar EUV illumination to the polar ionosphere could induce such difference due to conductivity changes. On the other hand, the solar wind also affects the SKR. On average, the SKR intensity is positively correlated with the solar wind dynamic pressure [e.g. Taubenschuss et al., 2006]. The SKR period also shows slight changes correlated with the solar wind on a time scale of 20–30 days [Zarka et al., 2007]. In summary, N– and S–SKR intensities have independent daily periodic modulations, but their values averaged over 10.7 h are temporally correlated and simultaneously react to the solar wind.

SKR also shows bursts whose durations are shorter than the SKR period, lasting for a few hours. Jackman et al. [2009] suggested their evolution processes as follows. First, magnetotail reconnection enhances the auroral field-aligned currents (FACs) of both hemispheres. When the current density exceeds the maximum value that magnetospheric electrons can carry without acceleration, a field-aligned electric field forms above the auroral region to sustain the current density. Accelerated electrons generate N– and S–SKR emissions with an upward extension of the auroral acceleration region [e.g., Cowley et al., 2005] associated with a low-frequency extension of SKR down to 50–100 kHz. This model can be compared to the terrestrial auroral kilometric radiation (AKR) bursts associated with substorms [Morioka et al., 2007]. Morioka et al. [2007] identified two distinct AKR source regions. One is at low altitude (4,000–5,000 km) corresponding to the main band AKR (300–500 kHz) and another is at high altitude (6,000–12,000 km) corresponding to the low-frequency AKR (30–150 kHz) formed only during the burst. Although the formation of a field-aligned acceleration region is not confirmed around Saturn [Menietti et al., 2011; Lamy et al., 2010], we expect that SKR bursts in both hemispheres can be simultaneously activated with FAC enhancement events. If the ratio of FACs between northern (winter–side) and southern (summer–side) hemispheres are controlled by the polar ionospheric conductivity, the flux ratio between N– and S–SKR can be similar in the normal status and the burst status.

In order to compare N– and S–SKR components simultaneously and to minimize the visibility effects associated with local time and latitude [Lamy et al., 2008], we analyzed data in 2005 DOY 250 – 2006 DOY 200 when Cassini stayed close to the equatorial plane. This interval corresponds to the southern summer when the asymmetry of N– and S–SKRs was clear. We selected isolated SKR burst events which are not contaminated by the enhancement of daily and longer variations. For this selection, we first derived the averaged spectral and flux profiles of normal 'non-burst' N– and S–SKR as a function of the N– and S–SKR phases, respectively. We then located the N– and S–SKR bursts which were enhanced over the averaged activity.

2 Data and methodology

2.1 SKR spectra data set

The SKR spectral data set was formed from the electric field data of the high frequency receiver (HFR) of Cassini RPWS [Gurnett et al., 2004]. The electric field antenna system consists of three nearly orthogonal monopole antennas (u, v, and w) with 10 m in length and 2.86 cm in diameter, where u and v can be operated as a dipole D. HFR covers 3.5 kHz–16 MHz and can measure complex auto- and cross-correlations between the three monopoles (u, v, and w) or dipole (D and monopole w). The polarization and source direction of the SKR is provided by an inversion process [Cecconi and Zarka, 2005]. In this procedure, received waves were assumed as pure circularly polarized waves, i.e., the Stokes parameters Q and U were zero, in order to reduce the number of inversion parameters for the two–antenna mode, D and w.

As Lamy et al. [2008] pointed out, the SKR data set contains the energy flux spectra ($W/m^2/Hz$) normalized to 1 AU from Saturn and the total emitted powers (W/str) covering the range 3.5–1,500 kHz, with 24 logarithmically spaced channels from 3.5 to 320 kHz ($f/df = 20$) and 24 linearly spaced channels of from 350 to 1500 kHz ($df = 50$ kHz). The circular polarization degree V was used to separate between the N– and S–SKR, with a positive V (LH polarization) as S–SKR and a negative V (RH polarization) as N–SKR. In this study, we eliminated data (a) dominated by the solar radiation, local electrostatic emissions, or artificial interferences, (b) with a low circular polarization ($|V| < 0.2$), or (c) with signal–to–noise ratio below 10 dB. The time resolution was set to 3 min. The observation time was corrected by the light travel time from Saturn to the spacecraft.

2.2 Data selection criteria

The SKR energy flux and spectral range depend on the spacecraft location, because of the non-uniform spatial distribution of SKR sources and and the hollow cone emission pattern [Lamy et al., 2008; Kimura et al., 2013]. SKR emissions are usually not observed in the equatorial shadow zone (ESZ), which extends in radial distance from Saturn out to 4–7 R_S, depending on frequency [Lamy et al., 2008]. The N– and S–SKR are mainly observed in the latitude of -20 – $+70$ deg and -60 – $+10$ deg, respectively [Kimura et al., 2013]. In observer's local time (LT), SKR is stronger in the dawn side sector, ∼2–10 h LT. In order to compare the N– and S–SKR bursts simultaneously, we selected the data obtained when Cassini was located outside the ESZ, close to the equator, and on the dawn side sector. We focused on the period from 2005 DOY 250 to 2006 DOY 200 and selected the proper data using the following criteria: (a) the kronocentric latitude in the $[-1°, +1°]$ range, (b) the radial distance larger than 10 R_S, and (c) the local time in 22–12 h LT. During this interval, 93% of the data satisfied these criteria. Examples of SKR bursts in this data set are shown in Figure 1. The isolated bursts are accompanied with a lower frequency extension below 50 kHz, enhanced from the 'normal' N– or S–SKR flux level.

The SKR normal activity level is modulated independently in each hemisphere at the associated SKR phase. Figure 2 (left) shows the SKR phase–frequency spectrogram of

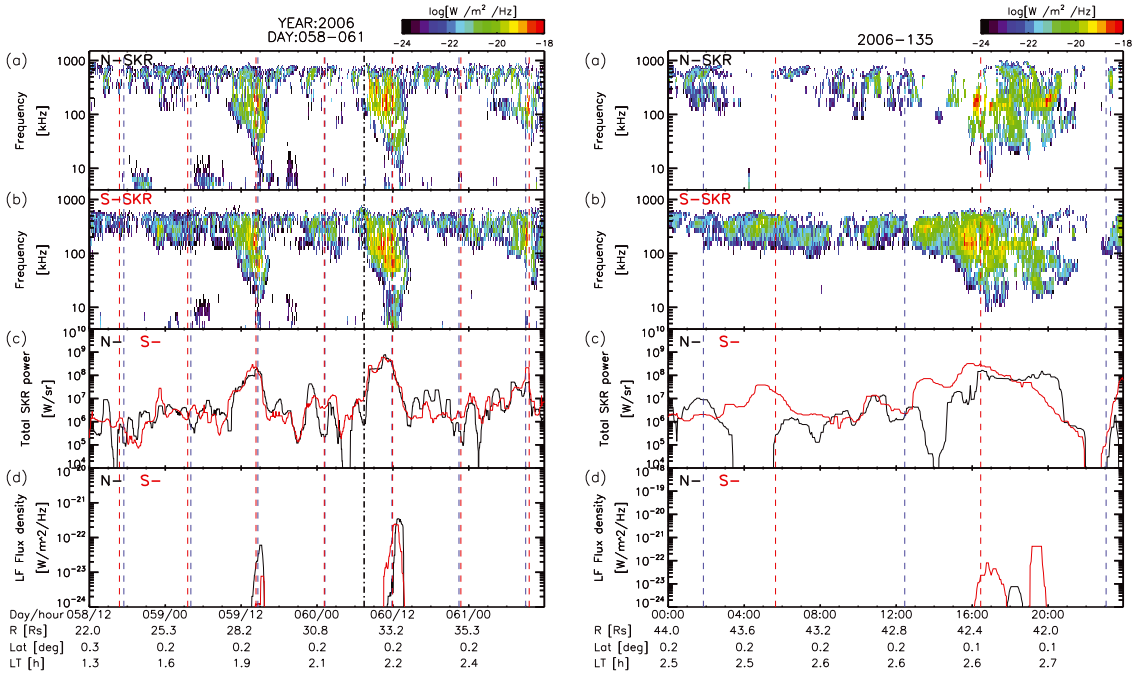

Figure 1: Example of simultaneous N– and S–SKR bursts. (a)(b) Dynamic spectra of the N– and S–SKR for the 3.5–1,500 kHz range, respectively, with the energy flux densities (W/m^2/Hz) normalized to 1 AU from Saturn and a time resolution of 3 minutes. (c)(d) Total SKR power (W/str) integrated for the 10–1,000 kHz range, and flux density for 10.12–45.56 kHz (W/m^2/Hz). Black and red lines represent the N– and S–SKR with 1 h median window. Blue and red vertical dashed lines show the timing when N– and S–SKR phases are close to 0 deg, respectively. The vertical dot–dashed line (7:30 on DOY 60) shows the reconnection timing from Jackman et al. [2014]. (Left) N– and S–SKR bursts at 13–15 h UT on DOY 59 and 11–13 h UT on DOY 60, 2006, when N– and S–SKR phases are almost synchronous. (Right) N– and S–SKR bursts at 16–18 h UT on DOY 135, 2006, when N– and S–SKR phases are not synchronous.

N– and S–SKR for the whole data set. The horizontal axis has a 10° spacing and the color contours correspond to the 75th percentile of the SKR flux densities. It clearly shows the correlation of N– and S–SKR to N– and S–SKR phase. Both strength and frequency range are maximum when the SKR phase was close to 0°, and minimum when the SKR phase was close to 180°, respectively.

We did a similar analysis for N– and S–SKR in the moving window of ±5 Saturn days, and derived the 75th percentile of the total power (W/str) in the 10–1000 kHz range, and the flux density (W/m^2/Hz) of the low-frequency SKR (LF–SKR) in the 10.12–45.56 kHz range, respectively. These values were used with the following two selection criteria for the isolated N– and S–SKR bursts: (1) Total N–SKR or S–SKR power was larger than the 75th percentile value within ±5 Saturn days in same N–SKR or S–SKR phase range. (2) LF N– or S–SKR power was larger than the 75th percentile value within ±5 Saturn days in same N–SKR or S–SKR phase range. With this method we identified the isolated short bursts in the data with daily modulation (independently in N– and S–SKRs) and longer variations (common in SKR from both hemispheres). In order to pick up clear

burst events, we also added two selection criteria: (3) No narrow-band emissions (n–SMR below 10 kHz or n–SKR in 10–40 kHz) identified, as no obvious gap between the main band SKR (96.65–400.0 kHz) and LF–SKR (10.12–45.56 kHz) was allowed. (4) The enhancement lasted more than 60 min, in order to pick up clear burst events.

Table 1 lists all isolated burst events identified by this method. The total number of identified isolated SKR burst events is 38. In 14 bursts, both N– and S–SKR satisfied the burst criteria. In 22 events, only S–SKR fulfilled the criteria. In the remaining 2 events, only N–SKR satisfied the criteria.

We briefly add the reason why some bursts only satisfy the burst criteria in a single hemisphere. The data set we used includes an artificial masking effect, with the SKR flux from the weaker hemisphere not being detected when the flux of the opposite hemisphere was continuously stronger. This resulted from the reduction logic of the Cassini RPWS/HFR. The time resolution of the integrated data set was 3 min, including the time shift of the light travel time from Saturn to the spacecraft. Each data sample included at least two full resolution samples. The RPWS/HFR full resolution samples from the spacecraft provided the dominant radio wave polarization for each time–frequency step. Hence, only the strongest RH (N–) or LH (S–) SKR component was detected. When both polarization components were observed at the same time with a similar intensity, the resulting polarization and flux were erroneous (faint polarization degree, wrong direction of arrival). Therefore, in the current data set, the data with an absolute circular polarization below 20 % was removed before integration. Unfortunately, this meant that when one hemispheric component was stronger than the other for the 3 min integration time, the flux of the weaker hemisphere was artificially determined as 0 [Cecconi, private communication]. Under the southern summer conditions studied in this paper, the S–SKR is generally more intense than the N–SKR [Lamy et al., 2008; Kimura et al., 2013]. Therefore, the N–SKR flux was frequently seen as 0, masked by the simultaneous stronger S–SKR. Although this is not a problem when studying the long-term averaged characteristics of the normal SKR, that is not the case for our SKR burst study. In the frequency–time diagram shown in Figure 1, the intensified frequency–time areas associated with a strong N– or S–SKR enhancement were always set to 'no flux' in the corresponding area of the weaker S– or N–SKR burst. We will try to escape from this problem by a simple method described in Appendix B of Fischer et al. [2015], which is now on-going.

3 Spectral and temporal profiles of the SKR bursts

Figure 2 (right) shows the median spectral profiles of N– and S–SKR bursts for 2 h before and after the onset time of 16 N– and 36 S–SKR bursts. The source altitude profiles are derived from the SKR frequency [Kimura et al., 2013].

The characteristics were similar for N– and S–SKR, except the difference in the peak flux level. In normal non-burst profiles, the SKR frequency range was limited to 100–700 kHz (1.5–0.3 R_S in altitude) for the N–SKR and to 50–600 kHz (2.1–0.3 R_S) for the S–SKR. The peak flux density was about $10^{-20.8}$ W/m^2/Hz for the N–SKR and about $10^{-19.8}$ W/m^2/Hz for the S–SKR at 100–200 kHz (1.5–1.0 R_S). In this interval, S–SKR

Table 1: Onset timings of 38 SKR bursts from DOY 250, 2005 to DOY 200, 2006. In 22 events, N–SKR bursts were not clear. In 2 events, S–SKR bursts were not clear.

Year–DOY	Time (UT)	N–SKR phase (deg)	S–SKR phase (deg)	comment
Iapetus	3561.3	79.331	718	1.21
2005–255	03:45	64	154	S–SKR burst: unclear
2005–258	20:09	190	222	
2005–277	11:51	286	28	N–SKR burst: unclear
2005–288	03:54	345	284	
2005–295	09:51	134	323	N–SKR burst: unclear
2005–295	19:30	102	285	N–SKR burst: unclear
2005–308	01:42	18	12	N–SKR burst: unclear
2005–308	09:48	293	282	N–SKR burst: unclear
2005–312	00:57	14	307	N–SKR burst: unclear
2005–315	07:51	175	57	N–SKR burst: unclear
2005–323	06:48	181	303	N–SKR burst: unclear
2005–340	11:21	157	16	
2005–361	11:33	8	266	N–SKR burst: unclear
2005–363	07:24	58	288	N–SKR burst: unclear
2006–001	22:33	139	313	
2006–015	01:24	37	10	N–SKR burst: unclear
2006–015	22:48	44	3	N–SKR burst: unclear
2006–024	21:51	150	332	N–SKR burst: unclear
2006–032	10:30	166	235	
2006–042	13:15	133	46	N–SKR burst: unclear
2006–047	16:39	6	199	N–SKR burst: unclear
2006–050	11:51	129	279	
2006–054	23:51	198	278	N–SKR burst: unclear
2006–059	13:36	326	336	
2006–060	10:30	316	313	
2006–070	09:27	154	357	
2006–076	20:27	22	122	N–SKR burst: unclear
2006–100	03:33	279	32	N–SKR burst: unclear
2006–103	23:51	201	227	N–SKR burst: unclear
2006–111	09:51	131	37	
2006–135	15:57	120	344	
2006–141	03:36	276	47	N–SKR burst: unclear
2006–146	23:18	345	18	S–SKR burst: unclear
2006–169	11:24	343	354	N–SKR burst: unclear
2006–187	13:15	324	32	
2006–193	07:03	326	297	N–SKR burst: unclear
2006–193	19:51	41	3	
2006–197	05:54	30	214	

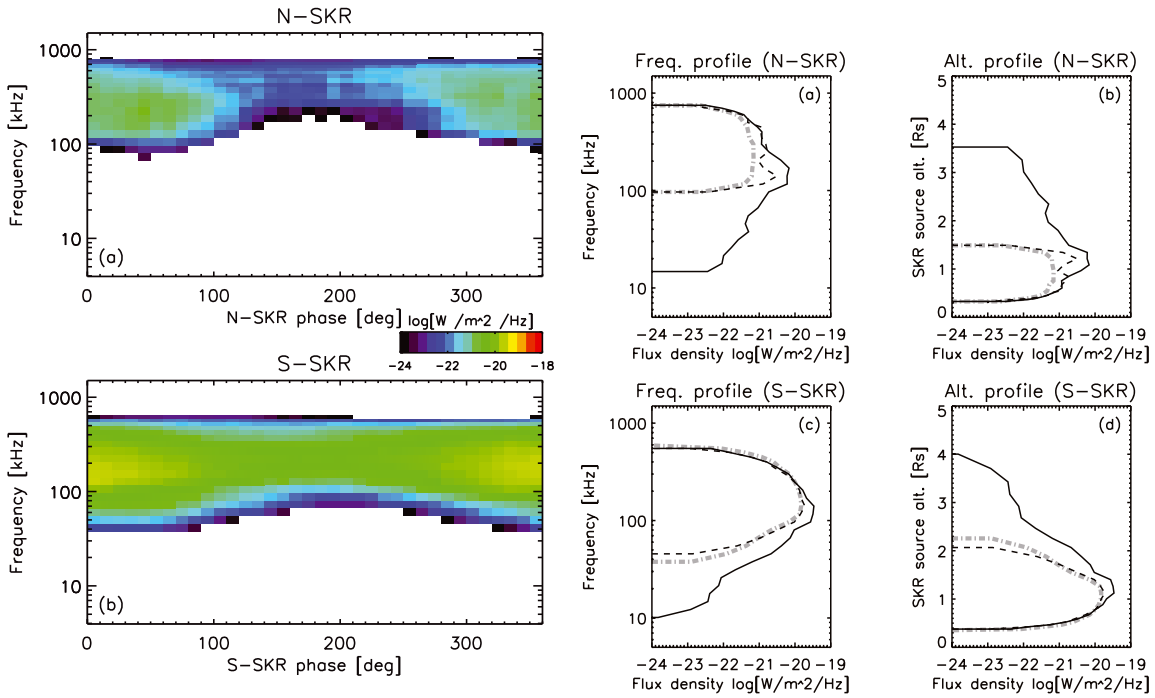

Figure 2: (Left) Dependence of N– and S–SKR spectra on N– and S–SKR phases from 2005 DOY 250 to 2006 DOY 200. The horizontal axis has a 10° spacing. The color contours correspond to the 75th percentile of the SKR flux densities. (Right) Frequency and source altitude profiles of (a)(b) N–SKR bursts and (c)(d) S–SKR bursts. The dashed and solid lines show the median profile for 2 h before and after the burst onset timings, respectively. The dot–dashed lines show the normal SKR profiles in the SKR phase of $0° \pm 30°$.

is about 10 times brighter than N–SKR. After the onset, the peak flux reached $10^{-20.2}$ W/m^2/Hz for the N–SKR and $10^{-19.4}$ W/m^2/Hz for the S–SKR at 100–200 kHz (1.5–1.0 R_S), keeping the difference to a factor of 6. The highest frequency and the lowest altitude of the source was similar even in the burst status.

During the SKR bursts, a lower frequency extension of SKR appeared in the 10–50 kHz range at higher altitudes (2–4 R_S), but no separation from the main band. In this frequency range, the flux density was not largely different. N–SKR bursts have an energy flux density of $10^{-21.2}$ W/m^2/Hz at 50 kHz (2 R_S) and $10^{-22.0}$ W/m^2/Hz at 30 kHz (3 R_S). S–SKR bursts have $10^{-20.8}$ W/m^2/Hz at 50 kHz (2 R_S) and $10^{-21.7}$ W/m^2/Hz at 30 kHz (3 R_S). The difference is a factor of 2–3, less than that in the main band. The lowest frequency and the highest altitude of the source were 20 kHz and 3.5 R_S, respectively.

Figure 3 left and right panels show the superposed time profiles of the N– and S–SKR bursts in ±8 hours around the onset of LF–SKR bursts. The median time profiles of the N– and S–SKR (red lines) commonly showed that the main band flux was gradually increased from 2–3 h before the onsets and gradually decreased till 2–3 h after that. The low frequency extensions became evident just from the onset and continued for 2–3 h. Similar time profiles, i.e., a preliminary main band enhancement and rapid subsequent low-frequency extension, were also seen in the AKR bursts [e.g. Morioka et al., 2007].

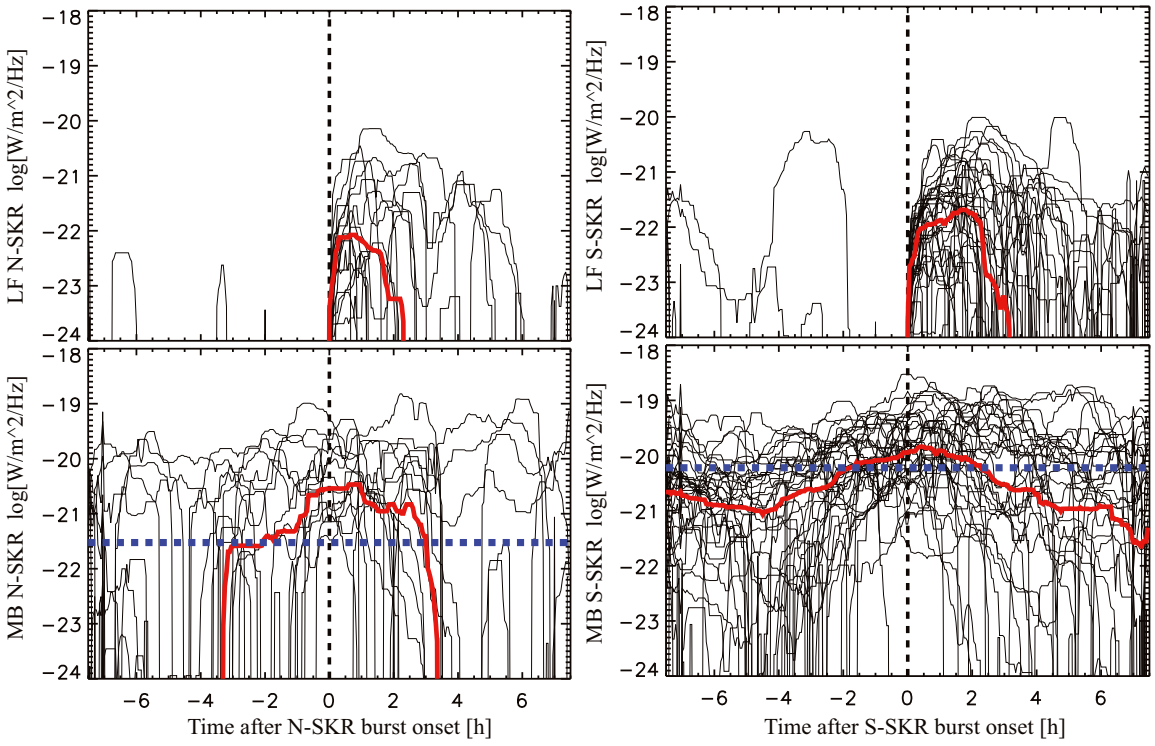

Figure 3: (Left) Time variations of N–SKR flux densities around the onset. The thin and red lines show the time profiles of 16 N–SKR bursts and their median, respectively. The top panel shows the low-frequency component (10.12–45.56 kHz). The bottom panel shows the main band component (96.65–400 kHz). The vertical dashed line at $t = 0$ indicates the burst onset timing. The blue dashed line shows the 75th percentile of the normal N–SKR in N–SKR phase of $0° \pm 30°$ as a reference. (Right) Same variations for 36 S–SKR bursts.

Although SKR has a longer time scale and does not display a dual source region, we can interpret the evolutions of SKR and AKR burst events based on a common process. The main band is emitted from the low altitude source and evolves steadily with longer duration, whereas the low frequency extension is emitted from the high altitude source and only appears during the short-term burst.

In the normal (non-burst) status (Figure 3, bottom panels), the characteristic of peak flux densities was similar to the one seen in Figure 2 (right). The typical flux density in the main band (100–400 kHz) was 10^{-21} W/m^2/Hz or less for N–SKR and 10^{-20} – 10^{-21} W/m^2/Hz for S–SKR. S–SKR is brighter than in N–SKR about 10 times. During the burst events 1–2 hours after the onsets, the main band flux is enhanced to $10^{-20.5}$ W/m^2/Hz for N–SKR and $10^{-19.8}$ W/m^2/Hz for S–SKR, which shows that S–SKR bursts is 5 times brighter than N–SKR bursts. A proposed origin of this north–south asymmetry is the enhancement of the ionospheric conductivity in the summer (southern) hemisphere, which leads to stronger FACs in the southern SKR source region [Lamy et al., 2009]. The flux difference in the main band was similar during the normal and burst status. This result supports the notion that the enhanced FAC during the burst events was divided between the northern and southern hemispheres. This division was not equal, but

maybe proportional to the different polar conductivities, in the burst status with larger FACs. This division ratio was similar but slightly less compared to the normal status. (It may be possible that enhanced FACs could heat up the polar ionosphere and reduce the conductivity difference of both hemispheres.)

In the lower frequency extension of SKR in the 10–50 kHz range (Figure 3, top panels), the flux during the burst status reaches $10^{-22.1}$ W/m^2/Hz for N–SKR and $10^{-21.7}$ W/m^2/Hz for S–SKR. The flux ratio of LF S–SKR bursts to N–SKR ones is 2–3, which is less than the ratio seen in the main band, as seen in the spectral profile of Figure 2 (right). If the difference in the main band SKR flux generated at lower altitudes is caused by the asymmetry of the FACs connected to the northern and southern auroral regions, we should also expect the higher altitude source region of the LF–SKR to have similar 'different FACs' on the same auroral field line. But, we note that the local time dependence of FACs seems unclear [Hunt et al., 2016]. Other factors should also be investigated. For example, it might be caused by the difference of their field lines, because the low frequency extensions are often observed to be separated from the main band. Although we consider that both are on a common field line in the studies of the two–step onset in AKR [e.g. Morioka et al., 2007], it would be valuable to confirm the source locations of simultaneous SKR components by direction–finding studies.

The SKR low-frequency extensions during the bursts could be caused by the extension of the source region to higher altitudes. We do not yet have a direct evidence that the enhancement of the field-aligned accelerations like at Earth are the origin of the LF–SKR from the high altitude source during the burst status. However, the LF–SKR is accompanied with the FAC enhancement which is seen as the main band SKR enhancement. The total power of AKR could be related to the auroral electrojet (AE) index [e.g., Morioka et al., 2012]. In the scenario connected to the current–driven instabilities, the top altitude of the field-aligned potential gap could be related to the FAC strength, which can be correlated to the main band AKR flux. We expect a similar scenario in the SKR case. The north–south asymmetry of the FACs at lower altitudes is seen in the SKR main band, and it can also cause a similar FAC asymmetry on the auroral field line extended to the higher altitudes. A reduction in flux difference between the lower frequency extension of the N– and S–SKR bursts suggests that the correlation of the FAC magnitudes to high altitude phenomena is non-linear. Cassini has explored Saturn's magnetosphere for more than 13 years and thus has coverage during two seasons. Accompanied with the study on the long-term flux changes of the SKR flux [Kasaba et al., 2017], further analysis and discussion will also be done for short-term bursts as an extension of this paper.

4 Summary

In this paper, we statistically investigated the energy flux ratio of N– and S–SKR during short-term bursts occurring in the Kronian southern summer. We identified 38 SKR burst events, including 16 northern and 36 southern bursts (14: both). The results are summarized as follows: (1) During the bursts for about 2 hours after the onsets, S–SKR in the main band (100–400 kHz) was 5–7 times stronger than N–SKR. This ratio was similar to (but slightly less than) the ratio in the non-burst normal status, i.e., the factor

10. The result suggests that auroral FACs in northern and southern polar region are similarly controlled by the different ionospheric conductances during normal and burst status. The maximum frequency (the lowest altitude of the SKR source region) is almost the same in N– and S–SKR in normal and burst status. (2) Less difference in the flux ration was seen in the low frequency extension (10–50 kHz) of SKR which only appeared in the burst status. The flux ratio of S–SKR to N–SKR in this frequency range is 2–3. The highest altitude is also similar between LF N– and S–SKR. It suggests that the the north–south asymmetry of the accelerated electrons in the higher altitudes is smaller.

Acknowledgments. The Editors thank David Andrews and one anonymous reviewer for their help in evaluating this paper.

References

Cecconi, B., and P. Zarka, Model of a variable radio period for Saturn, *J. Geophys. Res.*, **110**, A12203, doi:10.1029/2005JA011085, 2005.

Cowley, S. W. H., S. V. Badman, E. J. Bunce, J. T. Clarke, J.–C. Grard, D. Grodent, C. M. Jackman, S. E. Milan, and T. K. Yeoman, Reconnection in a rotation–dominated magnetosphere and its relation to Saturn's auroral dynamics, *J. Geophys. Res.*, **110**, A02201, doi:10.1029/2004JA010796, 2005.

Fischer, G., D. A. Gurnett, W. S. Kurth, S.–Y. Ye, and J. B. Groene, Saturn kilometric radiation periodicity after equinox, *Icarus*, **254**, 72–91, 2015.

Gurnett, D. A., et al. (29 co-authors), The Cassini radio and plasma wave investigation, *Space Sci. Rev.*, **114**, 396–463, 2004.

Gurnett, D. A., A. Lecacheux, W. S. Kurth, A. M. Persoon, J. B. Groene, L. Lamy, P. Zarka, and J. F. Carbary, Discovery of a north–south asymmetry in Saturn's radio rotation period, *Geophys. Res. Lett.*, **36**, L16102, doi:10.1029/2009GL039621, 2009.

Gurnett, D. A., J. B. Groene, T. F. Averkamp, W. S. Kurth, S.–Y. Ye, and G. Fischer, An SLS4 longitude system based on a tracking filter analysis of the rotational modulation of Saturn Kilometric Radiation, in *Planetary Radio Emissions VII*, edited by H. O. Rucker, W. S. Kurth, P. Louarn, and G. Fischer, Austrian Academy of Sciences Press, Vienna, 51–64, 2011.

Hunt, G. J., S. W. H. Cowley, G. Provan, E. J. Bunce, I. I. Alexeev, E. S. Belenkaya, V. V. Kalegaev, M. K. Dougherty, and A. J. Coates, Field-aligned currents in Saturn's magnetosphere: Local time dependence of southern summer currents in the dawn sector between midnight and noon, *J. Geophys. Res.*, **121**, 7785–7804, 2016.

Jackman, C. M., L. Lamy, M. P. Freeman, P. Zarka, B. Cecconi, W. S. Kurth, S. W. H. Cowley, and M. K. Dougherty, On the character and distribution of lower–frequency radio emissions at Saturn and their relationship to substorm–like events, *J. Geophys. Res.*, **114**, A08211, doi:10.1029/2008JA013997, 2009.

Kasaba, Y., et al., North–south asymmetry of Saturn's auroral radio emissions: The seasonal variation of their fluxes in half Kronian year, Japan Geoscience Union – American Geophysical Union Joint Meeting 2017, Chiba, Japan, 2017.

Kimura, T., L. Lamy, C. Tao, S. V. Badman, S. Kasahara, B. Cecconi, P. Zarka, A. Morioka, Y. Miyoshi, D. Maruno, Y. Kasaba, and M. Fujimoto, Long-term modulations of Saturn's auroral radio emissions by the solar wind and seasonal variations controlled by the solar ultraviolet flux, *J. Geophys. Res.*, **118**, 7019–7035, doi:10.1002/2013JA018833, 2013.

Kurth, W. S., T. F. Averkamp, D. A. Gurnett, J. B. Groene, and A. Lecacheux, An update to a Saturnian longitude system based on kilometric radio emissions, *J. Geophys. Res.*, **113**, A05222, doi:10.1029/2007JA012861, 2008.

Lamy, L., P. Zarka, B. Cecconi, R. Prangé, W. S. Kurth, and D. A. Gurnett, Saturn kilometric radiation: Average and statistical properties, *J. Geophys. Res.*, **113**, A07201, doi:10.1029/2007JA012900, 2008.

Lamy, L., B. Cecconi, R. Prangé, P. Zarka, J. D. Nichols, and J. T. Clarke, An auroral oval at the footprint of Saturn's kilometric radio sources, colocated with the UV aurorae, *J. Geophys. Res.*, **114**, A10212, doi:10.1029/2009JA014401, 2009.

Lamy, L., P. Schippers, P. Zarka, B. Cecconi, C. S. Arridge, M. K. Dougherty, P. Louarn, N. André, W. S. Kurth, R. L. Mutel, D. A. Gurnett, and A. J. Coates, Properties of Saturn kilometric radiation measured within its source region, *Geophys. Res. Lett.*, **37**, L12104, 2010.

Menietti, D., P. Schippers, O. Santolik, D. A. Gurnett, F. Crary, and A.J. Coates, Ion cyclotron harmonics in the Saturn downward current auroral region, *J. Geophys. Res.*, **116**, A12234, doi:10.1029/2011JA017102, 2011.

Morioka, A., Y. Miyoshi, F. Tsuchiya, H. Misawa, T. Sakanoi, K. Yumoto, R. R. Anderson, J. D. Menietti, and E. F. Donovan, Dual structure of auroral acceleration regions at substorm onsets as derived from auroral kilometric radiation spectra, *J. Geophys. Res.*, **112**, A06245, doi:10.1029/ 2006JA012186, 2007.

Morioka, A., Y. Miyoshi, N. Kitamura, H. Misawa, F. Tsuchiya, J. D. Menietti, and F. Honary, Fundamental characteristics of field-aligned auroral acceleration derived from AKR spectra, *J. Geophys. Res.*, **117**, A02213, doi:10.1029/2011JA017137, 2012.

Taubenschuss, U., H. O. Rucker, W. S. Kurth, B. Cecconi, P. Zarka, M. K. Dougherty, and J. T. Steinberg, Linear prediction studies for the solar wind and Saturn kilometric radiation, *Ann. Geophys.*, **24**, 3139–3150, 2006.

Zarka, P., L. Lamy, B. Cecconi, R. Prangé, and H. O. Rucker, Modulation of Saturn's radio clock by solar wind speed, *Nature*, **450**, 265–267, doi:10.1038/nature06237, 2007.